Li$_{2x}$BC$_3$: Prediction of a second MgB$_2$-class high-temperature superconductor

Yundi Quan ⬤ and Warren E. Pickett
Department of Physics, University of California Davis, Davis, California 95616, USA

Recent synthesis of Li$_{2x}$BC$_3$, pseudoisostructural to MgB$_2$, has been reported, with control of doping level by concentration x of Li. Density-functional calculations based on the virtual crystal approximation confirm metalization over a wide range of Li concentration but predict regions of structural instability. The electron-phonon coupling strength and superconducting critical temperature T_c around $x = 0.5$ is found to be comparable to that in MgB$_2$, but of different character, accounting for the unexpected result that a stronger bond-stretch mode and a higher B–C E$_g$ mode frequency results in little increase in T_c. The B–C honeycomb layer contributes strong σ-bonding (p_x, p_y) cylinders similar to MgB$_2$, while the corresponding C–C states lie well below the Fermi level and are dead" for coupling. However, the π-bonding (p_z) states on the B–C/C–C layer provide a large Fermi-level density of states and weak coupling that moderates the coupling strength and thereby T_c.

I. INTRODUCTION

Superconducting materials are comprised of several classes with widely differing characteristics that can be surveyed across each class to guide understanding of what properties are important in that class. MgB$_2$, discovered by Akimitsu's group [1] to superconduct at temperatures up to $T_c = 40$ K, remains a class with a single member. Calculations quickly established coupling by phonons to be the mechanism [2–7]. Attempts to increase T_c in this system by alloying have been unfruitful; strain can provide a minor increase [8]. However, theory indicates that phase-space scaling in two-dimensional (2D) metals is favorable [9–12] for promoting strong coupling, high T_c materials if the number of Fermi surfaces (FSs) can be increased while coupling strength is maintained.

Soon after that discovery, Rosner *et al.* [13,14] proposed that hole-doped Li$_{1-x}$BC ($x > 0$), which is effectively isostructural and nearly isovalent with MgB$_2$, could display T_c up to the 75K range. This material had been reported by Wörle *et al.* [15] but not measured to the necessary temperature to detect superconductivity. Attempts to reproduce such samples while retaining the crystal structure [16,17] have not been successful. Heating the stoichiometric crystals in an attempt to reduce the Li concentration leads to sudden loss of Li, with catastrophic consequences for the samples. Li$_x$BC thus adds to the list of promising superconductors for which experimental reproducibility has been a limitation; in effect, a phase boundary has been encountered.

More recently hole-doping of borocarbides has been approached through design of stoichiometric but metallic compounds of Li with B–C honeycomb layers. Bazhirov *et al.* studied Li$_2$B$_3$C and Li$_4$B$_5$C$_3$, both displaying σ-bonding bands crossing the Fermi level in MgB2 fashion [18]. They found strong coupling $\lambda = 1.18$ with predicted $T_c = 37$ K for the former, but moderate coupling $\lambda = 0.62$ and $T_c = 17$ K for the latter (for Coulomb pseudopotential $\mu^* = 0.10$). This

direction of design was extended by Gao *et al.* [19] with Li$_3$B$_4$C$_2$, in which the honeycomb layers contain B:C in 2:1 ratio. The predicted T_c was in the 40–55 K range, somewhat higher than in MgB$_2$. The same group designed a freestanding LiB$_2$C$_2$ trilayer [20]. Using the common isotropic procedure, the predicted T_c was around 40 K, but it was said that accounting for anisotropy in coupling, T_c was driven to the 100 K range (a much larger effect of anisotropy than has been obtained elsewhere). Strain of the trilayer was found to increase T_c. We are not aware of experimental progress on these predictions.

Milashius *et al.* [21] reported recently that induction melting of stoichiometric constituents produces honeycomb structure Li$_{2x}$BC$_3$, and that the concentration x of Li can be varied from 0.5 (LiBC$_3$) up to nearly one, filling nearly all of the Li sites in this structure (see below), which is a close variant of the LiBC, MgB$_2$, and graphene structures. Alternating C–C and B–C honeycomb layers are separated by Li sites, half of which are filled at the $x = 0.5$ LiBC$_3$ stoichiometry, see Fig. 1. In this paper, we provide evidence that a wide range of doping levels will be metallic with strong 2D features, and that superconductivity of LiBC$_3$ up to the 40 K regime occurs for carriers within the B–C layers.

Our structural model, from experiment, and computational methods are provided in Sec. II. Section III is devoted to a description of the electronic structure including the 2D FSs. The strength and character of electron-phonon coupling is described in Sec. IV. Section V provides information about the effect of Li concentration on T_c, and Sec. VI provides a summary of our findings.

II. METHODS AND CRYSTAL STRUCTURE

The structure consists of two graphene-structure layers C1–C3 and B–C2, separated by an interstitial Li layer [21]. The hexagonal lattice constants are $a = 2.541$ Å, $c =$
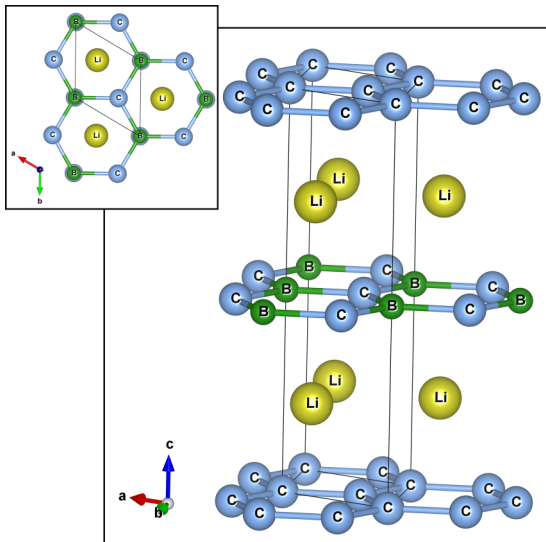
FIG. 1. Crystal structure of LiBC$_3$, illustrating the alternating C1–C3 and B–C2 honeycomb layers. The inset shows a top view, with the unit cell highlighted. Dark and light spheres in the layers represent B and C, respectively. Only half of the Li sites (yellow spheres, between the layers) shown are occupied at this stoichiometry, but the Li content, and resulting chemical potential and Fermi surfaces, can be varied up to nearly a Li occupation of two [21].

FIG. 2. Band structure of LiBC$_3$ near and below the Fermi level. The blue highlighted bands (left panel) indicate the σ-bonding bands in the metallic B–C2 layer that cross E_F near Γ. The thin black bands have C1–C3 character; those with σ-bonding character (red) lie about 4.5 eV below the corresponding B–C2 bands. The right panel emphasizes π-bonding bands (as noted).

7.599 Å. Li lies between the centers of the honeycomb midpoints and has variable occupancy as in alkali-intercalated graphite. Most data was presented for $\delta = 0.5$ in the designation Li$_{2\delta}$BC$_3$ (i.e., LiBC$_3$) but occupancy up to near $x = 1$ was possible [21]. The space group is hexagonal $P\bar{6}m2$ (No. 187), with the B–C alternation in the B–C2 layer lowering the symmetry from that of MgB$_2$.

In the following, we present results obtained from *ab initio* calculations using the pseudopotential code Quantum Espresso (QE) [22,23] with an energy cutoff of 60 Ry. For maximum uniformity, the cutoff and meshes have been kept uniform. The semi-local generalized gradient approximation of Perdew *et al.* [24] was the choice of exchange-correlation functional. The k mesh used in self-consistent calculations is $24 \times 24 \times 12$. Force constants in q space are obtained from linear response calculations on a $6 \times 6 \times 6$ Γ-centered q mesh. Dynamical matrices are then constructed from real space force constants and diagonalized to obtain phonon frequencies and vibrational eigenmodes. For electron-phonon coupling calculations, the q-mesh consists of $12 \times 12 \times 6$ points in the Brillouin zone shifted away from Γ point. Brillouin zone integration in electron-phonon coupling calculations is carried out using the optimized tetrahedron method [25] on a $24 \times 24 \times 12$ k mesh, sufficient since none of the FSs is tiny. The electron-phonon coupling with Wannier functions (EPW) codes were used for final zone samplings [26].

The partial occupation of the Li sites requires attention. We have applied the virtual crystal approximation (VCA) within the pseudopotential method. VCA and our uniform treatment of convergence parameters provides a realistic of variations with Li fraction x. For a given concentration x, each Li site is assigned a virtual atom pseudopotential, which is a composition-average of the Li and He

pseudopotentials: $V_{ps}^x = x V_{ps}^{\text{Li}} + (1 - x)V_{ps}^{\text{He}}$. Given that He simply binds strongly two electrons, this virtual atom will provide $2x$ electrons/f.u. to the B and C $s - p$ bands, and will enforce a realistic average spacing of the two adjacent layers. It should also retain the correct Madelung potential. This VCA treatment is a standard one for treating alloys in which neighbors in the periodic table share a single site, including carbon-based materials [27,28]. For each concentration, the lattice was relaxed so the correct phonon spectrum would be obtained.

III. ELECTRONIC STRUCTURE

The crystal structure of LiBC$_3$ consists of alternating layers of carbon-carbon and carbon-boron honeycomb layers, with partially occupied Li sites between. Interlayer coupling is weak as can be seen from flat dispersion of the bands along the k_z axis. The loosely stacked B–C and C–C layers results in bands that overlap in energy but with negligible interband mixing except from the Madelung potential, which simplifies our discussion.

The band structure plot of Fig. 2 highlights the strongly coupled B–C2 layer σ bonding bands crossing the Fermi level, of the type that is responsible for the superconductivity of MgB$_2$; even the amount of overlap of the Fermi level at Γ is similar. The Madelung potentials (and B–C chemistry) put the analogous, and parallel, bands in the C1–C3 layer at 4.5 eV lower energy, a large difference and one that, as mentioned above, removes them from participation in conduction or electron-phonon coupling except to provide strong bonding and contribute to the equilibrium volume and to phonon frequencies.

The FSs are displayed in Fig. 3. There are two roughly circular cylinders centered at Γ and having negligible k_z dispersion, even less than occurs in MgB$_2$ due to the larger separation of B–C2 layers. The radii can be obtained from
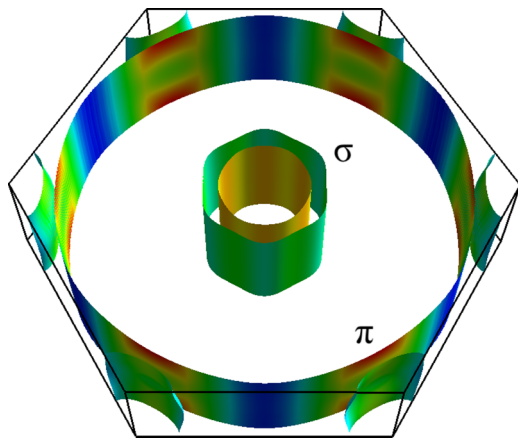
FIG. 3. Fermi surfaces of LiBC$_3$, with velocities displayed according to color. The two central cylinders are similar to those in MgB$_2$. The large cylinder arises from p_z orbitals.

FIG. 4. Partial and total density of states of LiBC$_3$ in the energy range from -10 eV to 4 eV. The individual projections are easy to interpret (viz., the van Hove singularities and two-dimensional step edges (but are hidden in the total.

Fig. 2. Two other surfaces appear. One is a very large cylinder. Its character consists of C1–C3 π-nonbonding orbitals, also with negligible k_z dispersion due to the lack of states in intervening B–C2 layer with which to mix. Finally, there are small K-point centered cylinders from states of similar character, also having 2D character. Studies of phase-space effects in 2D reveal [9] that the EPC coupling strength and thereby T_c are insensitive to the radii of such FS cylinders (i.e., the corresponding "carrier density"), but additional cylinders of any radius continue to add coupling strength.

The projected density of states (PDOS) onto C2 and B atomic spheres (also C1 and C3 atomic spheres) is presented in Fig. 4. Any contribution in the region of the Fermi level from Li is negligible. The in-plane dispersive σ bands extend over 11 eV. For $x = 0.5$ (Li sites half filled), the Fermi level lies, accidentally, in a high and narrow peak in the DOS associated with van Hove singularities in the C–C p_z band structure (as does H$_3$S at high pressure [29,30]), with calculated $N(E_F) = 0.56$ states/eV-spin. The Fermi level lies only 100 meV above the peak, so nonadiabatic effects will arise as in the case of H$_3$S [31].

With such a strong and narrow peak lying at the Fermi level, thermodynamic properties, including T_c, will be sensitive to the level of Li concentration, and that $x = 0.5$ provides the near-optimal Li concentration. The DOS decreases for higher Li concentrations and exhibits step discontinuities in energy reflecting the 2D character of the bands.

IV. ELECTRON-PHONON COUPLING

A. DEFORMATION POTENTIAL AND E_{2g} frequency

It is tempting to expect, due to their structural and electronic similarity, that LiBC$_3$ is enough like MgB$_2$ (and Li$_x$BC) that λ can be obtained reasonably from the E_{2g} (bond stretch) mode frequency and deformation potential as was done for those two compounds [2,13]. The EPC strength (see below) is of the two-band form $\lambda^\sigma + \lambda^\pi$. If the latter is small compared to the former, this comparison of the strong σ-bonding aspects of the three compounds should provide insight on how to optimize T_c. The ability to estimate this (dominant) contribution
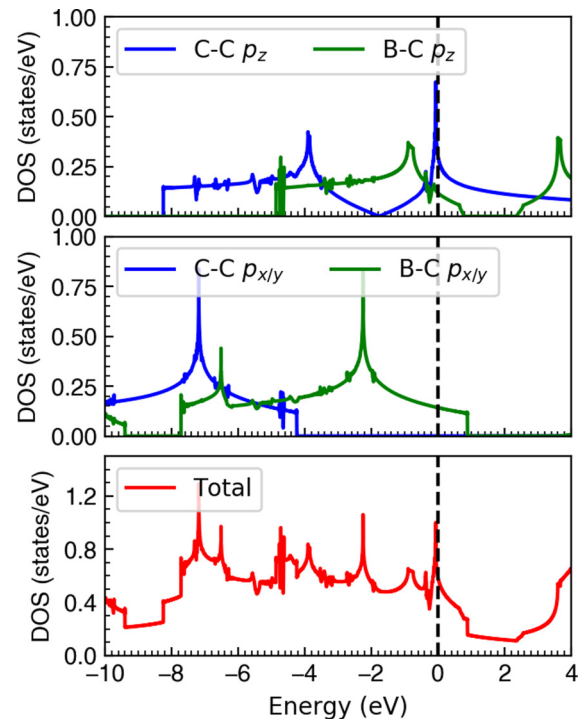
relies on the finding that, for cylindrical FSs of 2D bands, the integrated coupling strength of λ^σ is independent of the radius k_F [9]. The integral can be obtained in terms of an average squared matrix element over the FS, and for small cylinders this will be given by the deformation potential of the σ-bonding $p_x - p_y$ bands at the zone center.

First, the deformation potential $\mathcal{D}^\sigma$ of the B–C2 σ bands at Γ for the bond stretch vibration in the B–C2 plane was calculated in parallel with that of MgB$_2$, and also the density of states of the cylindrical FSs $N_\sigma(0)$, and the value of $M\omega^2$ for the bond-stretch E_{2g} mode. For LiBC and Li$_{2x}$BC$_3$, the mass in this formula will be the average of those of the common isotopes of B and C, hence $M = 11.5$ amu. The data are reported in Table I, using the published values for MgB$_2$ [2] and LiBC [13].

The σ-bonding mode deformation potential for the B–C2 layer in LiBC$_3$ ($x = 0.5$) at Γ is 20 eV/Å. This calculation was carried out as before for MgB$_2$ and Li$_x$BC, with the band splitting displayed in Fig. 5. For MgB$_2$, the corresponding value was 13 eV/Å; for Li$_{1-x}$BC, 18.5 eV/Å. Specifically, for this bond-stretch mode, the splitting of degenerate bands at Γ is $\delta\varepsilon_{k=0} = 0.8$ eV for bond-stretching displacements of the B and C2 atoms by 0.02 Å. The effect of this phonon on the splitting of the C1-C3 π-derived bands at E$_F$ is well over an order of magnitude smaller. This great difference is the signature of a two-gap superconducting state, large on the FS B–C2 σ bands near Γ and small on the B–C2 and C1–C3 π bands near the zone edge. The π states will have contributions from other phonon modes that may reduce the difference in gaps.

TABLE I. In-plane lattice constants a, and calculated parameters for the three layered compounds, *solely* from the σ-bonding Fermi surface cylinders, the corresponding bond stretch mode E_{2g}, and the corresponding deformation potential (hence not for comparison with experiment). Although the deformation potential $\mathcal{D}_{E_{2g}}$ is much larger for $LiBC_3$ than for MgB_2, thus providing strong coupling at high frequency, the high E_{2g} mode frequency makes the denominator $M\omega_{E_g}^2$ in λ^{σ} *much larger*, hence λ^{σ} is correspondingly reduced, along with T_c.

Compound	a (Å)	$\omega_{E_{2g}}$ (meV)	$\mathcal{D}_{E_{2g}}$ (eV/Å)	$N_{\sigma,\uparrow}$ (eV^{-1} spin^{-1})	$M\omega_{E_{2g}^2}$ (10^3 amu meV^2)	λ^{σ}	T_c^{σ} (K)
MgB_2	3.08	58	13	0.110	37	1.00	42
$Li_{0.5}BC$	2.75	68	18.5	0.143	53	1.80	107
$LiBC_3$	2.54	110	20	0.140	139	0.83	50

The calculated zone center B–C2 E_{2g} bond stretch harmonic phonon energy is $\omega = 110$ meV (see the next section), much higher than the 58–68 meV for the other two
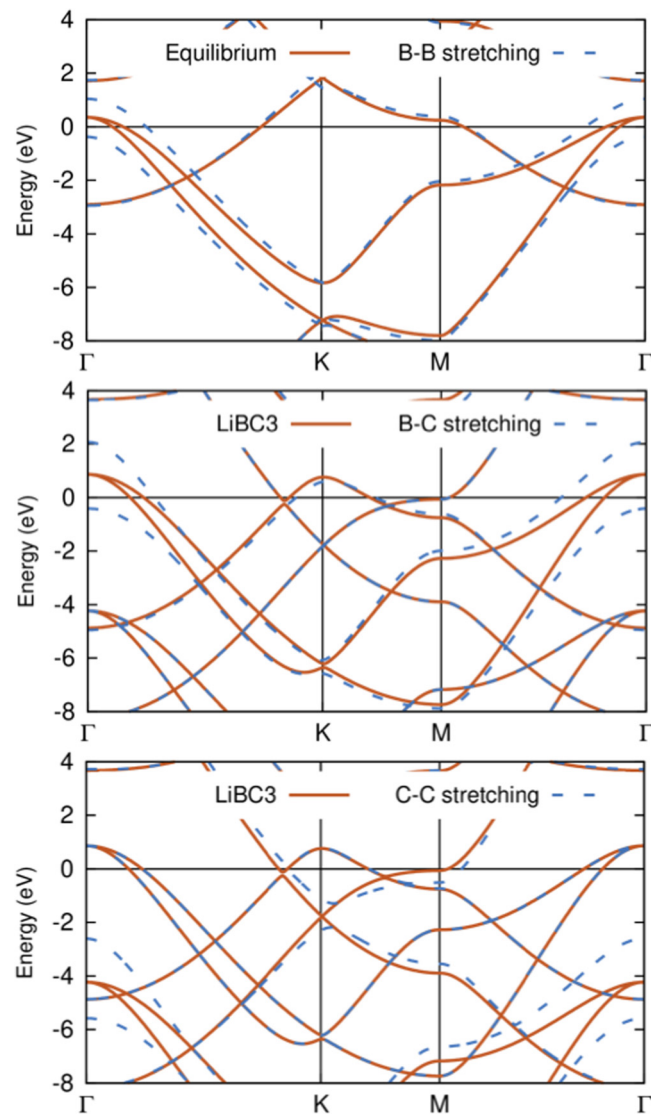
FIG. 5. Illustrations of deformation potentials, which are the band splittings at Γ near the Fermi level (taken as the zero of energy). Top panel: Deformation potential of MgB_2 B-B stretching mode; middle panel: $LiBC_3$ B–C bond stretching mode; bottom panel: $LiBC_3$ C-C bond stretching mode. The bond stretch is identical in each panel.

compounds. Since $M\omega^2$ appears in the denominator of the σ coupling strength

$$\lambda^{\sigma} \propto \frac{N_{\sigma,\uparrow}(0)\mathcal{D}_{E_{2g}}^2}{M\omega_{E_{2g}}^2}, \tag{1}$$

the value of λ^{σ} is reduced accordingly. The high frequency does, however, contribute separately to raising T_c by setting the scale of T_c. For the value of T_c^{σ} (the hypothetical value from the σ bands alone), $\omega_{E_{2g}}$ appears in the prefactor and compensates the decrease in λ^{σ}. The increase in the E_{2g} frequency can be ascribed to the compressive strain on the B–C2 bond length arising from the pure C (C1–C3) separation in $LiBC_3$, which is 16% less than in MgB_2 (30% smaller unit cell area). This is an extreme example of a case in which one layer of a material applies compressive strain (pressure) on another layer, and in this case the active B–C2 layer is compressed and the frequency and the deformation potential are increased dramatically.

To observe in a consistent manner the effect on T_c^{σ}, the Allen-Dynes equation [32] for strong coupling is used, using the stretching mode data only. The σ-bonding data, using the data from An and Pickett [2] and Rosner et al. [13] for MgB_2 and $Li_{0.5}BC$, respectively, are presented in Table I, using $\mu^* = 0.13$ in all cases for uniformity. The results are for an Einstein mode at $\omega_{E_{2g}}$, the deformation potential from Fig. 5, and the mean atomic mass in the B–C layer (whose small differences are included but not of consequence). The high frequency of $LiBC_3$ is the positive prefactor in the Allen-Dynes equation, but appearing in the denominator it reduces λ^{σ} to become more comparable to that of MgB_2. The resulting T_c^{σ} is 50K, only 25% larger than MgB_2. $Li_{0.5}BC$ is calculated to have T_c somewhat in excess of 100 K in this rough approximation, with the lower phonon frequency increasing λ to 1.8, which more than compensates the smaller prefactor in T_c. Below we will see that this E_{2g} estimate of T_c is misleading.

B. LATTICE DYNAMICS OF LiBC₃

The relevant results incorporating all effects requires the evaluation of the phonon spectrum and electron-phonon coupling to obtain the Eliashberg function $\alpha^2 F(\omega)$. The phonon spectrum for $LiBC_3$ ($x = 0.5$) calculated from QE is displayed along symmetry lines in Fig. 6, with atom-projected densities of states provided in the right-hand panels. The spectrum has minor q_z dispersion ($\Gamma - A$ line) except for the acoustic modes, where it is required for structural stability. The in-plane acoustic modes cross low-frequency Li optic modes
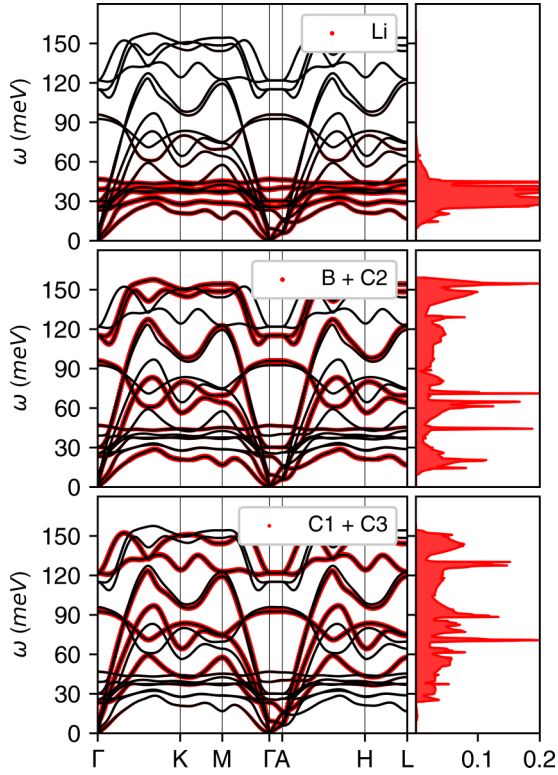
FIG. 6. Phonon dispersion curves of LiBC$_3$, weighted by atomic contribution (as labeled) pictured in red. The Kohn anomalies in the upper branches around Γ are signaled by abrupt dips in the dispersion curves, and comparable in strength to those in MgB$_2$. Lithium modes (top panel) have low frequencies and provide minor coupling (see Fig. 7), while the C1 + C3 modes in the lower panel make an important contribution to coupling, otherwise dominated by B–C2 modes.

and extend to high frequency. Li modes are, in spite of the small mass of Li, low in frequency and reflect weak force constants on the Li ions. There is small weight (hard to resolve numerically) in the low-frequency region due to the large sound velocities, providing little phase space and no impact on the physics.

The nearly dispersionless modes in the 25–50 meV range are Li vibrations, with the flatness reflecting essentially localized vibrations of Li ions (small force constants). There is weak coupling in this frequency range, see Fig. 7. The in-plane longitudinal acoustic mode cuts through various optic modes, extending up to the 120 meV range. The hardest C1–C3 and B–C2 bond stretch modes extend to 155 meV; recall that the Raman active bond stretch mode in diamond is around 160 meV, indicating the very large force constants in LiBC$_3$ in spite of some metallic screening.

C. ELECTRON-PHONON COUPLING IN LiBC$_3$

The FS-averaged Eliashberg spectral function $\alpha^2 F(\omega)$ is displayed in the top panel of Fig. 7. Much of the contribution to T_c lies in a hump from 110–150 meV, with lesser contributions to T_c from 20–30 meV, around 60 meV, and 85–100 meV. The lower frequencies contribute disproportionately to $\lambda = \int \frac{2}{\omega} \alpha^2 F(\omega) d\omega$, but the lower frequency gives them
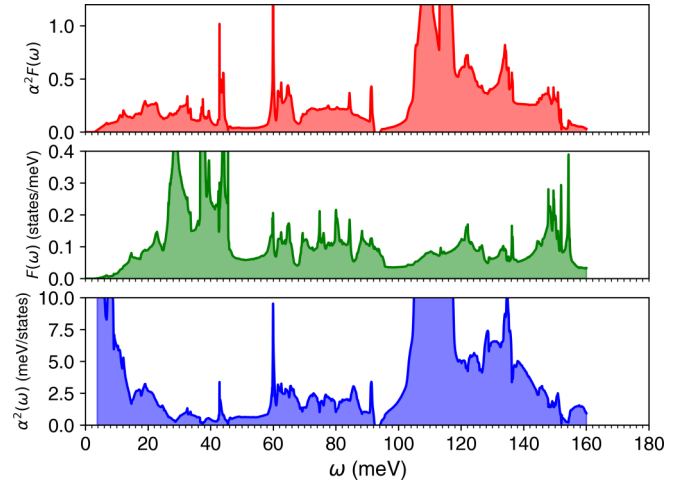
FIG. 7. The Eliashberg spectral function $\alpha^2 F(\omega)$, top panel; the phonon density of states $F(\omega)$, and $\alpha^2(\omega)$, for LiBC$_3$, from top to bottom. Sharp narrow peaks do not have specific significance. Much of the contribution to T_c arises from the 110–150 meV region of high-frequency vibrations, with additional contribution from the 85–100 meV region. The low frequency 15–30 meV modes will contribute to λ but will contribute little to T_c (see text). $\alpha^2(\omega)$ below 10 meV is subject to large numerical uncertainty.

less impact in contributing to T_c. The conventional Eliashberg integral leads to $\lambda = 0.88$, other materials characteristics are provided in Table II.

Also provided in Fig. 7 is the phonon DOS $F(\omega)$ and the coupling strength ratio $\alpha^2(\omega) = \alpha^2 F(\omega)/F(\omega)$. $\alpha^2(\omega)$ reveals several features: seemingly very strong coupling to acoustic modes (look at 15 meV and below) but numerically uncertain due to the limited number of acoustic modes in the sampling; some coupling to an anomalously low-frequency B–C mode in a narrow range centered at 20 meV; smaller coupling to some C1–C3 modes which have only π-bonding character at the Fermi level. These latter weakly coupled modes include half of the hardest vibrations, in the 150–160 meV range, because the C1–C3 layer σ states lie well below the Fermi level. The bulk of the contribution to T_c arises from the B–C2 modes in the 90–150 meV range.

The frequency moments, calculated with respect to the normalized shape function $g(\omega) = 2\alpha^2 F(\omega)/\lambda\omega$, provided in Table II, are much lower than the bond-stretch modes around 120 meV, illustrating how the ω^{-1} factor emphasizes the lower frequencies when there is some coupling at low ω. With

TABLE II. Variation with x of the properties relevant to T_c, for the Li$_{2x}$BC$_3$ alloy system.

x	λ	$\omega_{\log}$ (meV)	ω_1 (meV)	ω_2 (meV)	T_c (K)
0.50	0.88	63	83	95	34
0.60	0.64	72	87	96	17
0.75	0.53	81	96	105	9
0.80	0.17	99	107	112	0
0.90	0.23	92	101	109	0
1.00	0.23	71	82	92	0
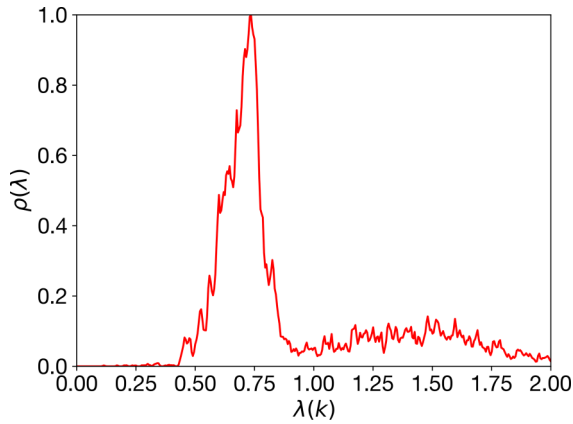
FIG. 8. Distribution of electron-phonon coupling strengths λ_{nk}, with k near the Fermi surface. The distribution is characteristic of a weak bimodal form, see text.

$\mu^* = 0.13$, the predicted T_c is no more than 35 K. This value is much smaller than what might have been expected from the $\mathcal{D}^2$ factor discussed in the previous subsection.

D. COUPLING STRENGTH ACROSS THE FERMI SURFACES

Electron-phonon coupling strength at a given k point is defined as, suppressing band indices,

$$\lambda_{\vec{k}} = \frac{1}{N(E_F)} \sum_{\vec{q},\nu} \omega_{\vec{q},\nu} \left| g_\nu^{SE}(\vec{k}, \vec{q}) \right|^2 \delta(\epsilon_{\vec{k}+\vec{q}}) \qquad (2)$$

$$= \sum_{k'} \lambda_{k,k'} \delta(\varepsilon_{k'}) / \sum_{k'} \delta(\varepsilon_{k'}). \qquad (3)$$

The second expression defines (implicitly) the FS decomposition of scattering processes from $\vec{k}'$ to $\vec{k}$ ($\lambda_{k,k'}$ and thus the anisotropy of coupling around the FSs. The distribution of λ_k, displayed in Fig. 8, is characteristic of a bimodal distribution: moderate coupling values in the 0.5–0.8 range, with a strong narrow peak centered at 0.7, and strong coupling values in the $1.1 < \lambda < 1.8$ range. These two regimes serve to produce the final value to $\lambda = 0.88$. This bimodal distribution shows similarity to that of MgB$_2$.

Survey of the contributions reveals, as expected, that values on the two B–C σ FSs cluster around 1.5, whereas those on the $B - C2$ and $C1 - C3$ π-bonding surfaces do not vary much from an average of 0.7. In this case, a two-band distribution of coupling leads to an instructive two-gap model [7,33] when studying thermodynamic and spectroscopic properties.

V. VARIATION WITH LITHIUM CONCENTRATION

The experimental report indicates that the Li concentration x can be varied from 0.5 to nearly one [21]. We have applied the virtual crystal approximation to the system Li$_{2x}$BC$_3$. The pseudopotential of Li$_{2x}$ was chosen as x times that of Li (valence one) and $1 - x$ times that of He (valence zero); increasing x increases the electron concentration. A few points on the resulting λ versus x diagram are shown in Fig. 9. For hole doping with respect to LiBC$_3$ ($x = 0.5$), coupling increases but the lattice quickly becomes unstable, an
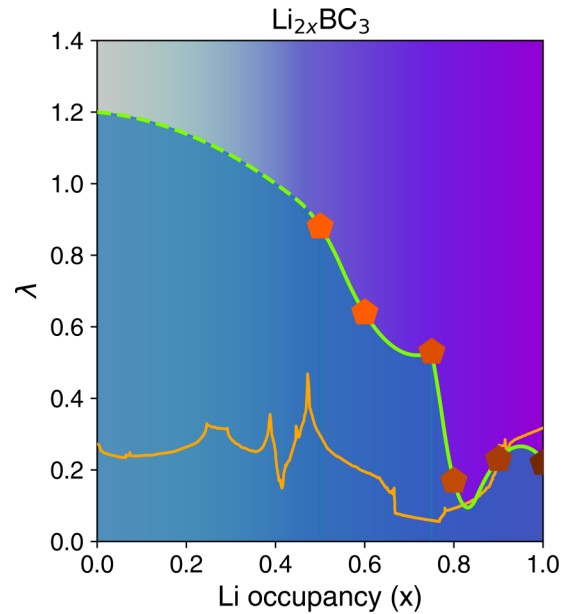
FIG. 9. Schematic $\lambda - x$ phase diagram of Li$_{2x}$BC$_3$. The orange line gives the Fermi level density of states N(E$_F$, x), for each value of x, obtained from a rigid band N(E) for $x=0.5$. The large red pentagons give λ at calculated values of x. In this figure, $x = 0.5$ represents LiBC$_3$. Decreasing x leads to lattice instability (dashed line), where coupling becomes even stronger. Adding Li beyond $x = 0.5$ leads to weaker coupling and disappearance of superconductivity, largely due to the decrease in the density of states.

unfortunate but common occurrence for systems with strong coupling near an optimum value.

The calculated materials characteristics versus x are presented in Table II, with the density of states N(E) also presented in the phase diagram of Fig. 9. Note that as x is lowered to 0.45 at a peak in N(E), the structure becomes unstable. Such instabilities associated with high $N(E_F)$ are familiar features. However, this lattice instability continues past the peak in the density of states, indicating that other processes are in play–other aspects of lattice instability arise even in moderately coupled metals.

Conventionally, one would expect $\lambda(x)$ to follow $N(E_F; x)$ for moderate values of changes in x, however, the sharp structure and peak in $N(E)$ is due to a van Hove singularity in the moderately coupled C1–C3 bands, whereas the strong coupling is more strongly affected by the B–C2 coupling and density of states. Our calculations indicate that the "stoichiometric" concentration LiBC$_3$ is near the maximum value of coupling with a stable lattice, and hence of the superconducting critical temperature.

VI. SUMMARY

LiBC$_3$ differs from Li$_{1-x}$BC and MgB$_2$ by having a larger deformation potential arising from B–C bond stretch modes coupling to corresponding B–C σ bonding states at the FS. These aspects are similar to those of MgB$_2$, but the deformation potential is 50% larger, traceable to the B–C bond compression enforced by the strongly bonded C–C layer. The (renormalized) bond stretch frequency also is larger. These

two characteristics, reflecting stronger coupling at higher frequency, should (naively) lead to an impressive increase in T_c. However, simple electron-phonon coupling is more complicated than that. The coupling strength λ is *decreased* by the higher frequency, a well-known consequence that is not very widely understood. If λ decreases while $\langle \omega^2 \rangle$ increases, the effect on T_c can peak and begin to decrease [10]. However, this is not really the whole answer.

LiBC$_3$ comes with a complication: only half (structurally) of the volume of LiBC$_3$ is contributing to EPC with the strong bond stretching coupling. There is a large density of states of the other half of the volume (C1–C3 layer) that is contributing with smaller coupling but a larger Fermi level density of states. This "additional" coupling, which according to simple pictures should be a positive factor, does not enhance T_c, but instead regulates it. The resulting value of T_c is similar to that of MgB$_2$. This result suggests that the volume contribution to superconductivity is an important consideration. This feature may become relevant to the observation of moderate to high T_c values being reported for thin, even monatomic layer, systems.

[1] J. Nagamatsu, N. Nakagawa, T. Muranaka, Y. Zenitani, and J. Akimitsu, Superconductivity at 39 K in magnesium diboride, Nature **410**, 63 (2001).

[2] J. M. An and W. E. Pickett, Superconductivity of MgB$_2$: Covalent Bonds Driven Metallic, Phys. Rev. Lett. **86**, 4366 (2001).

[3] J. Kortus, I. I. Mazin, K. D. Belashchenko, V. P. Antropov, and L. L. Boyer, Superconductivity of Metallic Boron in MgB$_2$, Phys. Rev. Lett. **86**, 4656 (2001).

[4] Y. Kong, O. V. Dolgov, O. Jepsen, and O. K. Andersen, Electron-phonon interaction in the normal and superconducting states of MgB$_2$, Phys. Rev. B **64**, 020501 (2001).

[5] K.-P. Bohnen, R. Heid, and B. Renker, Phonon Dispersion and Electron-Phonon Coupling in MgB$_2$ and AlB$_2$, Phys. Rev. Lett. **86**, 5771 (2001).

[6] T. Yildirim, O. Gülseren, J. W. Lynn, C. M. Brown, T. J. Udovic, Q. Huang, N. Rogado, K. A. Regan, M. A. Hayward, J. S. Slusky, T. He, M. K. Haas, P. Khalifah, K. Inumaru, and R. J. Cava, Giant Anharmonicity and Nonlinear Electron-Phonon Coupling in MgB$_2$: A Combined First-Principles Calculation and Neutron Scattering Study, Phys. Rev. Lett. **87**, 037001 (2001).

[7] A. Liu, I. I. Mazin, and J. Kortus, Beyond Eliashberg Superconductivity in MgB$_2$: Anharmonicity, Two-Phonon Scattering, and Multiple Gaps, Phys. Rev. Lett. **87**, 087005 (2001).

[8] A. V. Pogrebnyakov, J. M. Redwing, S. Raghavan, V. Vaithyanathan, D. G. Schlom, S. Y. Xu, Q. Li, D. A. Tenne, A. Soukiassian, X. X. Xi, M. D. Johannes, K. Kasinathan, W. E. Pickett, J. S. Wu and J. C. H. Spence, Enhancement of Superconducting Transition Temperature in MgB$_2$ by a Strain-Induced Bond-Stretching Mode Softening, Phys. Rev. Lett. **93**, 147006 (2004).

[9] W. E. Pickett and P. B. Allen, Superconductivity and phonon softening. III. Relation between electron bands and phonons in Nb, Mo, and their alloys, Phys. Rev. B **16**, 3127 (1977).

[10] W. E. Pickett, Electron-phonon coupling in MgB$_2$-like materials: Its magnitude and its limits, Braz. J. Phys. **33**, 695 (2003).

[11] W. E. Pickett, Design for a room temperature superconductor, J. Supercond. Novel Magn. **19**, 291 (2006).

[12] W. E. Pickett, The next breakthrough in phonon-mediated superconductivity, Physica C **468**, 126 (2008).

[13] H. Rosner, A. Kitiagorodsky, and W. E. Pickett, Prediction of High T_c Superconductivity in Hole-Doped LiBC, Phys. Rev. Lett. **88**, 127001 (2002).

[14] J. M. An, S. Y. Savrasov, H. Rosner, and W. E. Pickett, Extreme electron-phonon coupling in boron-based layered superconductors, Phys. Rev. B **66**, 220502(R) (2002).

[15] M. Wörle, R. Nesper, G. Mair, M. Schwarz, and H. G. V. Schnering, Z. Anorg. Allg. Chem. **621**, 1153 (1995).

[16] A. M. Fogg, J. Meldrum, G. R. Darling, J. B. Claridge, and M. J. Rosseinsky, Chemical control of electronic structure and superconductivity in layered borides and borocarbides: Understanding the absence of superconductivity in Li$_x$BC, J. Am. Chem. Soc. **128**, 10043 (2006).

[17] A. M. Fogg, G. R. Darling, J. B. Claridge, J. Meldrum, and M. J. Rosseinsky, The chemical response of main-group extended solids to formal mixed valency: The case of Li$_x$BC, Philos. Trans. R. Soc. A **366**, 55 (2007).

[18] T. Bazhirov, Y. Sakai, S. Saito and M. L. Cohen, Electron-phonon coupling and superconductivity in Li-intercalated layered borocarbide compounds, Phys. Rev. B **89**, 045136 (2014).

[19] M. Gao, Z.-Y. Lu, and T. Xiang, Prediction of phonon-mediated high-temperature superconductivity in Li$_3$B$_4$C$_2$, Phys. Rev. B **91**, 045132 (2015).

[20] M. Gao, X.-W. Yan, Z.-Y. Lu, and T. Xiang, Strong-coupling superconductivity in LiB$_2$C$_2$, trilayer films, Phys. Rev. B **101**, 094501 (2020).

[21] V. Milashius, V. Pavyuk, K. Kluziak, G. Dmytriv, and H. Ehrenberg, LiBC$_3$: A new borocarbide based on graphene and heterographene layers, Acta Cryst. C **73**, 984 (2017).

[22] P. Giannozzi, S. Baroni, N. Bonini, M. Calandra, R. Car, C. Cavazzoni, D. Ceresoli, G. L. Chiarotti, M. Cococcioni, I. Dabo *et al.*, QUANTUM ESPRESSO: A modular and open-source software project for quantum simulations of materials, J. Phys.: Conden. Matter **21**, 395502 (2009).

[23] P. Giannozzi, O. Andreussi, T. Brumme, O. Bunau, M. Buongiorno Nardelli, M. Calandra, R. Car, C. Cavazzoni, D. Ceresoli, M. Cococcioni *et al.*, Advanced capabilities for materials modeling with Quantum ESPRESSO, J. Phys.: Condens. Matter **29**, 465901 (2017)

[24] J. P. Perdew, K. Burke, and M. Ernzerhof, Generalized Gradient Approximation Made Simple, Phys. Rev. Lett. **77**, 3865 (1996).

[25] M. Kawamura, Y. Gohda, and S. Tsuneyuki, Improved tetrahedron method for the Brillouin zone integration applicable to response functions, Phys. Rev. B **89**, 094515 (2014).

[26] S. Poncé, E. R. Margine, C. Verdia, and F. Giustino, EPW: Electron-phonon coupling, transport and superconducting properties using maximally localized Wannier functions, Comp. Phys. Commun. **209**, 116 (2016).

[27] K.-W. Lee and W. E. Pickett, Superconductivity in Boron-Doped Diamond, Phys. Rev. Lett. **93**, 237003 (2004).

[28] X. Blase, Ch. Adessi, and D. Connétable, Role of the Dopant in the Superconductivity of Diamond, Phys. Rev. Lett. **93**, 237004 (2004).

[29] Y. Quan and W. E. Pickett, Van Hove singularities and spectral smearing in high-temperature superconducting H_3S, Phys. Rev. B **93**, 104526 (2016).

[30] R. Akashi, Archetypical "push the band critical point" mechanism for peaking of the density of states in three-dimensional crystals: Theory and case study of cubic H_3S, Phys. Rev. B **101**, 075126 (2020).

[31] Y. Quan, S. S. Ghosh, and W. E. Pickett, Compressed hydrides as metallic hydrogen superconductors, Phys. Rev. B **100**, 184505 (2019).

[32] P. B. Allen and R. C. Dynes, Transition temperature of strong-coupled superconductors reanalyzed, Phys. Rev. B **12**, 905 (1975).

[33] H. J. Choi, M. L. Cohen, and S. G. Louie, Anisotropic Eliashberg theory of MgB_2: T_c, isotope effects, superconducting energy gaps, quasiparticles, and specific heat, Physica C **385**, 66 (2003).

[34] J. Towns, T. Cockerill, M. Dahan, I. Foster, K. Gaither, A. Grimshaw, V. Hazlewood, S. Lathrop, D. Lifka, G. D. Peterson, R. Roskies, J. R. Scott, N. Wilkins-Diehr, XSEDE: Accelerating scientific discovery, Comput. Sci. Eng. **16**, 62 (2014).